



# CHORUS

This is the accepted manuscript made available via CHORUS. The article has been published as:

## Correlations between the instantaneous velocity gradient and the evolution of scale-to-scale fluxes in two-dimensional flow

Yang Liao and Nicholas T. Ouellette

Phys. Rev. E **92**, 033017 — Published 29 September 2015

DOI: [10.1103/PhysRevE.92.033017](https://doi.org/10.1103/PhysRevE.92.033017)

# Correlations between the instantaneous velocity gradient and the evolution of scale-to-scale fluxes in two-dimensional flow

Yang Liao<sup>1</sup> and Nicholas T. Ouellette<sup>2,3,\*</sup>

<sup>1</sup>*Department of Geology & Geophysics, Yale University, New Haven, CT 06520, USA*

<sup>2</sup>*Department of Mechanical Engineering & Materials Science, Yale University, New Haven, CT 06520, USA*

<sup>3</sup>*Department of Civil and Environmental Engineering, Stanford University, Stanford, CA 94305, USA*

Using high-resolution particle tracking velocimetry and filter-space techniques, we study the links between the scale-to-scale transfer of energy and enstrophy and instantaneously rotational and straining regions, as determined by the classic Okubo–Weiss parameter, in a quasi-two-dimensional laboratory flow. Although the Okubo–Weiss parameter has shortcomings, we find that, when suitably conditioned, it is surprisingly a good predictor for the future evolution of the spectral fluxes. By studying Lagrangian correlation functions, we explain our findings by showing that both the spectral fluxes and the Okubo–Weiss parameter are independently correlated for long times along fluid-element trajectories, and thus that any predictive capacity of the Okubo–Weiss parameter arises because it is coupled to fluid advection. Our results suggest potential strategies for forecasting in complex flows by looking for quantities with long Lagrangian correlation times.

PACS numbers: 47.27.De, 47.10.Fg, 47.27.T-

## I. INTRODUCTION

Fluid motion is often highly spatiotemporally complex; but even at extremely high Reynolds numbers, it is not unstructured. Instead, unsteady and turbulent flows tend to organize spontaneously into spatially extended regions of distinct character that persist for macroscopic times. Because of this tendency, which must be rooted in the nonlinear dynamics of the Navier–Stokes equations, a large body of work has been built up over the years aimed at pinpointing and characterizing such coherent structures [1]. Although coherent structures were first studied in the context of flow visualization, they are also thought to have promise for modeling complex flows [2].

Building a viable model based on coherent structures, however, requires understanding the role played by the chosen structures in the dynamics of the system [3]. For describing turbulent flows, we must characterize how structures contribute to or interact with the scale-to-scale cascade processes that make turbulence a distinct state of flow. Typically, these spectral cascades are treated in Fourier space, as this is the natural way to tease apart multi-scale processes. Once we take a Fourier transform, however, we lose all information about the spatial variation of the velocity field—and thus cannot connect the spectral dynamics to a description of the flow in terms of coherent structures. Here, therefore, we take a different approach based on so-called filter-space techniques [4–11], which allow the spatial localization of spectral processes.

Previously [12], we studied how the scale-to-scale flux of energy in a quasi-two-dimensional weakly turbulent flow was related to so-called Lagrangian coherent structures (LCSs) [13], and showed that LCSs tend to divide

regions of the flow field with different spectral character [14]. Current methods for calculating LCSs, however, require knowledge of the future evolution of the flow, and thus our results on the connection between LCSs and spectral flux cannot be used to forecast how the flux will change in time. Here, therefore, we consider a much simpler kind of coherent structure that can be computed instantaneously. We use the classic Okubo–Weiss parameter  $\Lambda = \det \nabla \mathbf{u} = (s^2 - \omega^2)/4$ , where  $s^2$  is the square of the strain rate and  $\omega^2$  is the enstrophy ( $\omega$  is the vorticity), to partition the flow field into regions that are dominated by rotation ( $\Lambda < 0$ ) and those that are dominated by strain ( $\Lambda > 0$ ) [15, 16].

Although there are some theoretical issues with the use of the Okubo–Weiss parameter as a criterion for partitioning the flow field (such as its non-invariance under some kinds of reference-frame boosts [17] or an implicit assumption that the velocity gradient evolves slowly compared to the vorticity gradient [18]), it has the advantages of being simple both to compute and to interpret and relying only on instantaneous information. Thus, it can be measured in complex geophysical flows where finely resolved long-time flow data may not be available, precluding the measurement of more intricately defined coherent structures [19]. Additionally, previous work on connecting structure and spectral dynamics has shown that the sign of  $\Lambda$  does indeed correlate with differences in the flux of enstrophy between scales [8]. Here, we expand on this work and consider the scale-to-scale fluxes of both energy and enstrophy in our quasi-two-dimensional laboratory flow. We show that not only does the sign of  $\Lambda$  correlate with differences in these fluxes, but that these differences persist in time—and thus that an instantaneous measurement of the Okubo–Weiss field may allow some limited forecasting of the evolution of the local spectral properties of the flow. We explain this result by measuring the Lagrangian autocorrelation function of  $\Lambda$ , finding that  $\Lambda$  remains correlated along fluid-element trajectory-

---

\* nto@stanford.edu

ries for appreciable lengths of time. Combined with our previous results demonstrating similar long correlations for the spectral fluxes [12] as well as recent theoretical results on the correlation of scalar fields with Lagrangian advection [20], our results indicate that the persistence of many flow properties for individual fluid elements may be useful for designing forecasting methods.

We begin below in Sec. II with a description of our experimental apparatus and procedures and the analysis tools we use. We then present our results in Sec. III, including the statistics of the scale-to-scale energy and enstrophy fluxes conditioned on the sign of the Okubo–Weiss parameter, measurements of their persistence along trajectories, and the Lagrangian correlation functions of  $\Lambda$ . Finally, we summarize and discuss some of the implications of our measurements in Sec. IV.

## II. METHODOLOGY

### A. Experimental Details

We generate quasi-two-dimensional flow in the laboratory using an electromagnetically stirred thin layer of electrolytic fluid. We have described the apparatus in detail elsewhere [11, 21–23], and so we only give a brief description here. We place a layer of salt water (16% NaCl by mass in deionized water) 5 mm deep on top of a glass plate. The lateral extent of the salt-water layer is  $86 \times 86 \text{ cm}^2$ . Beneath the glass is a square array of permanent neodymium-iron-boron magnets arranged in stripes of alternating polarity. Since the salt-water layer is electrically conductive, we drive steady electric current through it using a current-controlled power supply connected to a pair of copper bar electrodes that are immersed in the fluid. The combination of the electric current and the magnetic field produce a Lorentz body force that drives flow. At low currents, the flow is locked to the symmetries of the magnet array; for alternating stripes such as we use here, the low-current flow is a pattern of alternating shear bands typically known as a Kolmogorov flow [24]. As the current is increased, however, the flow breaks free of the imposed symmetry and becomes (weakly) turbulent [24]. To compare different flow conditions, we define a Reynolds number  $\text{Re}$  based on the measured in-plane root-mean-square velocity  $U$ , the kinematic viscosity of the salt water  $\nu$ , and the spacing between the magnets  $L_m$ , which roughly sets the scale of energy injection into the flow. For the data presented here, taken with an electric current of 1.25 A, we measure  $\text{Re} = UL_m/\nu = 270$ . At this Reynolds number, the flow is energetic enough to be spatiotemporally complex and not constrained by the magnets, while still remaining reliably two-dimensional [21]. We note, however, that this Reynolds number should really be viewed as a nondimensionalization of the electric current [25], rather than as a measure of any turbulent scale separation. Further details, including the global energy spectrum of the flow

and a detailed analysis of the scale-to-scale energy and enstrophy transfer, are given in Ref. [23].

To measure the flow field, we use particle tracking velocimetry (PTV). We seed the fluid with  $50\text{-}\mu\text{m}$ -diameter fluorescent polystyrene microspheres that absorb in the blue and fluoresce in the green. The particles have a specific gravity of 1.05, and so rise to the surface of the salt water; to avoid surface-tension-driven interaction between them, we float a 5 mm layer of pure water on top of the salt water. On the time scale of our experiments (typically a few minutes), salt diffusion between the layers is not a factor. The upper surface of the pure-water layer is free, and the pure water is undriven (since the electric current flows only through the salt water).

We image the particles with an IDT MotionPro M5 camera mounted above the apparatus at a frame rate of 60 frames per second. The data set analyzed here consists of 5000 frames, or about 83 s. The  $2320 \times 1728$  pixels on the camera detector correspond to an imaged area of  $31.7 \times 23.6 \text{ cm}^2$  (roughly  $12.5 \times 9 L_m$ ), which we position in the center of the apparatus, far from any wall effects. Thus, the portion of flow we measure is open and unbounded. We track the motion of about 30 000 particles per frame using a multi-frame predictive tracking algorithm [26], and measure the particle velocities by convolving the resulting trajectories with a smoothing and differentiating kernel [27]. We then construct velocity fields from the individual particle locations and velocities by projecting them onto a basis of streamfunction eigenmodes [21], which both removes noise and ensures that the measured fields are two-dimensional.

### B. Filtering and Spectral Fluxes

To measure the spatially localized spectral properties of the flow, we use so-called filter-space techniques (FSTs) that reveal the coupling between scales by suppressing the small-scale variation of the flow field [4–11]. We construct filtered flow observables by convolving the experimentally measured fields with a function that acts as a low-pass filter in Fourier space. The  $i^{\text{th}}$  component of the filtered velocity field, for example, is given by

$$u_i^{(r)}(\mathbf{x}) = \int G(\mathbf{x} - \mathbf{x}'; r) u_i(\mathbf{x}') d\mathbf{x}', \quad (1)$$

where  $G$  is the filter kernel and the superscript  $(r)$  denotes the length scale below which the variation is suppressed. Any function that acts as a low-pass filter will work in an FST, and the results are typically insensitive to the exact filter shape [7, 12]. Here, we used a round finite impulse response filter constructed by convolving a sharp spectral filter with the desired frequency cutoff with a Gaussian window function.

The utility of filtering becomes apparent when we write the equations of motion for the filtered kinetic energy  $E^{(r)} = (1/2)u_i^{(r)}u_i^{(r)}$  and enstrophy  $\Omega^{(r)} = (1/2)\omega^{(r)}\omega^{(r)}$ ,

where  $\omega$  is the vorticity (a scalar in two dimensions). Starting from the Navier–Stokes equations, one can write

$$\frac{\partial E^{(r)}}{\partial t} = -\frac{\partial J_i^{(r)}}{\partial x_i} - \nu \frac{\partial u_i^{(r)}}{\partial x_j} \frac{\partial u_i^{(r)}}{\partial x_j} - \Pi^{(r)} \quad (2)$$

and

$$\frac{\partial \Omega^{(r)}}{\partial t} = -\frac{\partial K_i^{(r)}}{\partial x_i} - \nu \frac{\partial \omega^{(r)}}{\partial x_i} \frac{\partial \omega^{(r)}}{\partial x_i} - Z^{(r)}. \quad (3)$$

Here,  $J_i^{(r)}$  and  $K_i^{(r)}$  are spatial currents of (filtered) energy and enstrophy, respectively, and contain contributions to spatial transport from advection, pressure stresses, and viscous diffusion; their analytical expressions are

$$J_i^{(r)} = \frac{1}{\rho} u_i^{(r)} p^{(r)} + u_i^{(r)} E^{(r)} - \nu \frac{\partial E^{(r)}}{\partial x_i} + u_j^{(r)} \left[ (u_i u_j)^{(r)} - u_i^{(r)} u_j^{(r)} \right] \quad (4)$$

and

$$K_i^{(r)} = u_i^{(r)} \Omega^{(r)} - \nu \frac{\partial \Omega^{(r)}}{\partial x_i} + \omega^{(r)} \left[ (u_i \omega)^{(r)} - u_i^{(r)} \omega^{(r)} \right], \quad (5)$$

where  $\rho$  is the fluid density,  $p$  is the pressure, and  $\nu$  is the kinematic viscosity.

The terms proportional to  $\nu$  are direct dissipation terms. Analogues to these currents and dissipation terms also appear in the equations of motion for the full energy and enstrophy. The final terms on the right-hand sides of these equations are new, however, and encode the coupling between the resolved scales and those that have been suppressed. These terms are given by

$$\Pi^{(r)} = - \left[ (u_i u_j)^{(r)} - u_i^{(r)} u_j^{(r)} \right] \frac{\partial u_i^{(r)}}{\partial x_j} \quad (6)$$

and

$$Z^{(r)} = - \left[ (u_i \omega)^{(r)} - u_i^{(r)} \omega^{(r)} \right] \frac{\partial \omega^{(r)}}{\partial x_i}, \quad (7)$$

and directly measure the flow of energy and enstrophy, respectively, from scales larger than  $r$  to those smaller than  $r$ . With the sign convention we have chosen, positive values of these spectral fluxes denote transfer to smaller scales, while negative values denote transfer to larger scales. Importantly, both  $\Pi^{(r)}$  and  $Z^{(r)}$  are functions of space, and can be defined locally; thus, they give us a way to connect the spectral properties of the flow with the spatial properties. Finally, we note that the filtering operation is a post-processing step; thus, unlike in large-eddy simulation where the filter scale is chosen at the outset, we can re-filter our data with whatever  $r$  we choose, so long as it is appreciably larger than the resolution limit of our data [28].

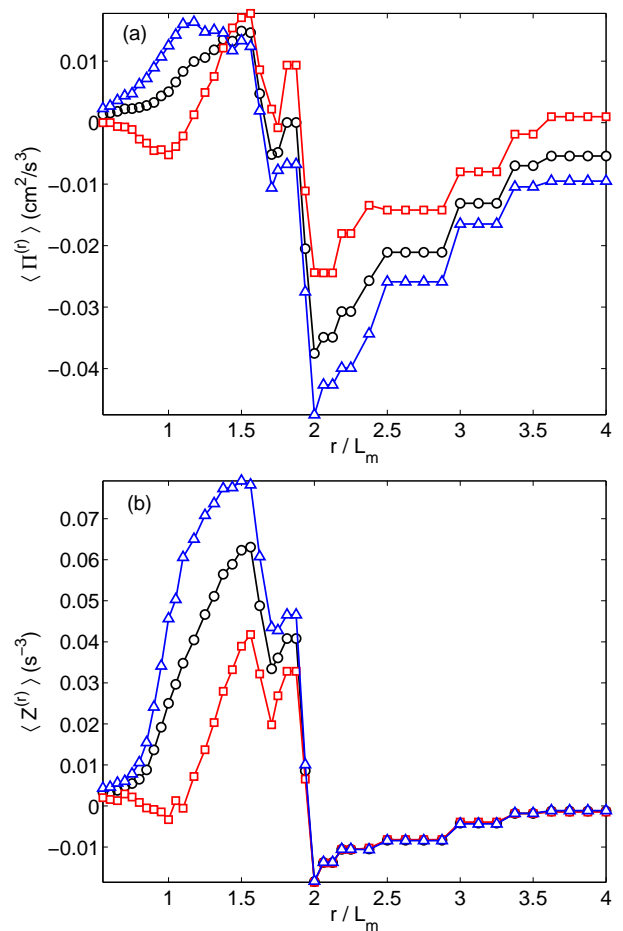


FIG. 1. (Color online) Conditional mean values of the (a) energy and (b) enstrophy fluxes as a function of the filter scale  $r$  normalized by the magnet spacing  $L_m$ . Red squares denote mean values conditioned on being in rotational regions, while blue triangles denote those conditioned on being in straining regions. Black circles show the unconditional means.

### III. RESULTS

#### A. Conditional Moments of Spectral Fluxes

For fully developed two-dimensional turbulence, the Kraichnan–Leith–Batchelor phenomenology predicts that we should observe two spectral cascade processes [29–31], unlike the single Kolmogorov–Richardson energy cascade found in three-dimensional turbulence: one cascade of enstrophy from the scale of energy injection  $L_{inj}$  to smaller scales, where it is dissipated by viscous action, and an inverse cascade of energy from  $L_{inj}$  to larger scales, where it is dissipated by large-scale frictional processes.

In Figure 1, we plot the the measured mean energy and enstrophy fluxes  $\langle \Pi^{(r)} \rangle$  and  $\langle Z^{(r)} \rangle$ , where the angle brackets denote averaging over space and time (where we weigh space and time equally in the average), as a function of the filter scale  $r$ . As we have reported before

[21, 23], we see average behavior that is consistent with expectations. We find an energy injection scale of  $L_{inj} \approx 1.8L_m$ . The energy flux (Figure 1(a)) is largest for  $r > L_{inj}$ , where it is negative (flowing to large scales in an inverse cascade, given our sign convention). Since our turbulence is not fully developed, there is some leakage of energy to small scales [7], and we do not observe an inertial range with constant energy flux. The enstrophy flux, in contrast, is large and positive for  $r < L_{inj}$  (Figure 1(b)), flowing to small scales, with little leakage to large scales. As an aside, we note that since our turbulence is not fully developed, long scaling ranges are not required to produce the correlations we describe below.

Previously, Chen *et al.* [8] reported that in the enstrophy cascade, regions of the flow field with different signs of the (filtered) Okubo–Weiss parameter had different enstrophy flux characteristics, and that the net forward cascade of enstrophy was primarily active in straining regions with  $\Lambda^{(r)} > 0$ . In Figure 1, then, we also plot the mean energy and enstrophy fluxes conditioned on the sign of  $\Lambda^{(r)}$ . Just as Chen *et al.* reported, we see a non-negligible effect, although one that is different for different filter scales. Strain appears to enhance the dominant fluxes we see (the inverse flux of energy and the forward flux of enstrophy) relative to rotation. For the leakage fluxes of energy and enstrophy we observe, however, the picture is somewhat less clear.  $\Lambda^{(r)}$  has very little impact on the mean enstrophy flux for scales larger than  $L_{inj}$ , and does not show uniform behavior for the energy flux below  $L_{inj}$ .

The mean energy and enstrophy fluxes, however, do not give a complete picture of the spectral dynamics in the flow. Since the net energy and enstrophy cascades are the result of a small imbalance in positive and negative flux, the local values of  $\Pi^{(r)}$  and  $Z^{(r)}$  can be orders of magnitude larger than the mean values [8, 11, 12]. We therefore also computed the conditional skewnesses (that is, the normalized third moments, e.g.  $\langle \Pi^{(r)3} \rangle / \langle \Pi^{(r)2} \rangle^{3/2}$ ) of  $\Pi^{(r)}$  and  $Z^{(r)}$  to study the asymmetry in the sign of the flux. Note that Chen *et al.* [8] also observed more skewed distributions of  $Z^{(r)}$  in straining regions in the enstrophy cascade. As shown in Figure 2, we do see an effect of  $\Lambda^{(r)}$  on the skewnesses for both energy and enstrophy, and the picture is somewhat different from the story told by the mean values shown in Figure 1. For the enstrophy, both the mean flux and its skewness are enhanced in straining regions relative to rotational regions. For the energy, however, the flux is marginally more skewed in *rotational* regions, even though its mean value is enhanced in straining regions, although the effect of  $\Lambda^{(r)}$  on the energy flux skewness is not large.

## B. Spatiotemporal Persistence

We have shown that the sign of  $\Lambda^{(r)}$  can be used to glean some information about the nature of the local spectral dynamics, and in particular that regions where

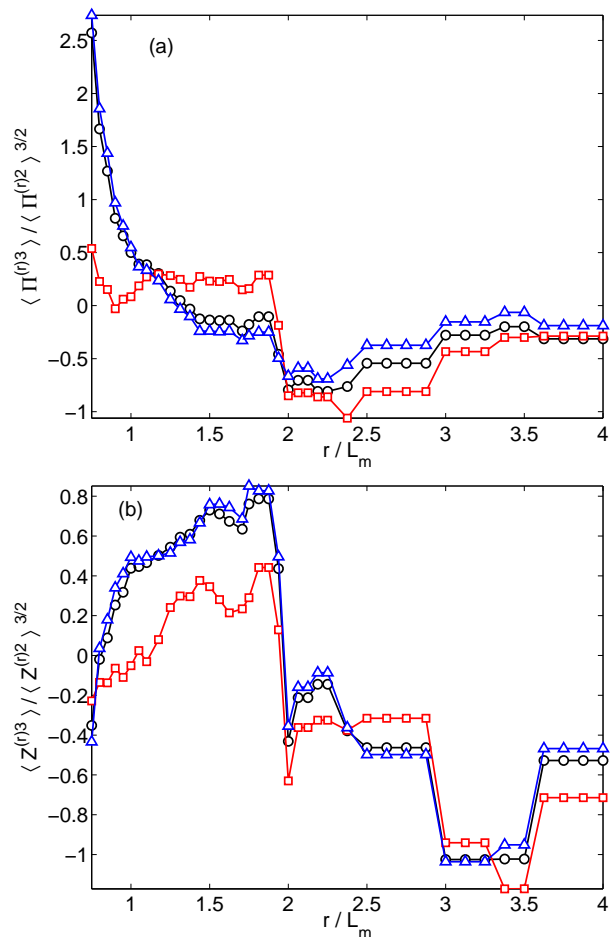


FIG. 2. (Color online) Conditional skewness (normalized third moments) of the (a) energy and (b) enstrophy fluxes as a function of the filter scale  $r$  normalized by the magnet spacing  $L_m$ . Red squares denote rotational regions, while blue triangles denote straining regions. Black circles show the unconditional skewnesses.

strain dominates rotation tend to be associated with more intense spectral transfer. Knowing about the instantaneous state of the flow, however, is of limited utility; if we hope to use coherent structures to forecast the evolution of the flow, we must ensure that our instantaneous observations persist in time.

One could try to assess the temporal persistence of the effects we have seen by considering, for example, the way  $\Pi^{(r)}$ ,  $Z^{(r)}$ , and  $\Lambda^{(r)}$  vary at fixed locations. But any such Eulerian measures of persistence will be dominated by large-scale sweeping, and will often reveal more about the mean flow than the subtleties of the turbulent dynamics. Instead, therefore, we consider the Lagrangian averages of the energy and enstrophy fluxes [14]; that is, we measure the average value of  $\Pi^{(r)}$  and  $Z^{(r)}$  along the trajectories of fluid elements (computed using the full, unfiltered velocity fields), calculating functional integrals

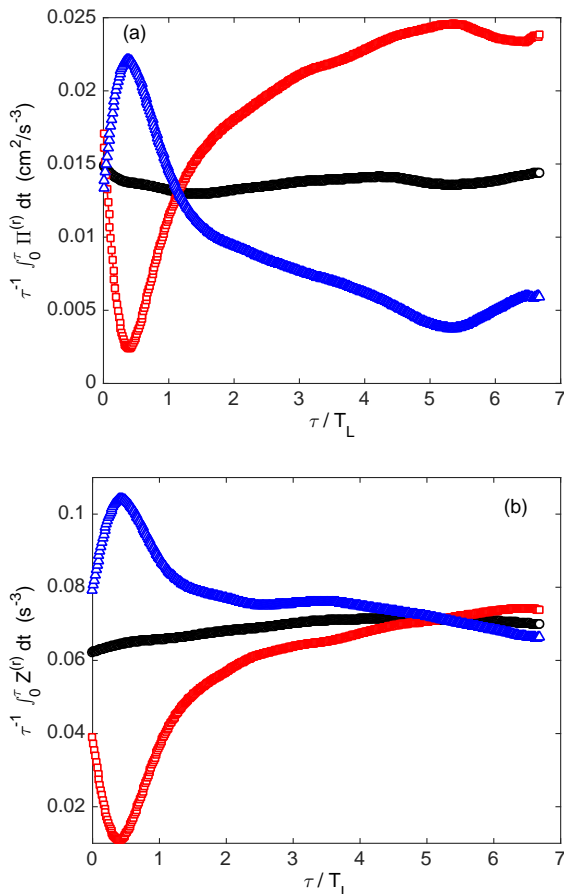


FIG. 3. (Color online) Time evolution of the Lagrangian averages of the (a) energy and (b) enstrophy fluxes at a fixed filter scale of  $r = 1.5L_m$ . Black circles denote unconditional averages; red squares are averages taken over particles that were initially (at  $\tau = 0$ ) in rotational regions, while blue triangles are for those that were initially in straining regions.

of the form

$$\frac{1}{\tau} \int_0^\tau \Pi^{(r)}(\mathbf{X}(t)) dt, \quad (8)$$

where the integral is taken over the Lagrangian trajectory  $\mathbf{X}(t)$ . We have shown previously that this kind of averaging can reveal the advective structure of the flow, and that the Lagrangian-averaged energy flux correlates well with the spatial distribution of Lagrangian coherent structures [14]. Lagrangian averaging is also closely related to so-called mesochronic analysis [32], which has its underpinnings in ergodic theory [33].

In Figures 3 and 4, we show the Lagrangian averages of the energy and enstrophy fluxes as a function of the averaging time  $\tau$  for two different filter scales:  $r = 1.5L_m$ , where the forward enstrophy flux is most intense (Figure 3), and  $r = 2L_m$ , where the inverse energy flux is largest (Figure 4). We computed the averages using 6006 trajectories with initial locations placed evenly throughout the flow domain. For both cases, the Lagrangian aver-

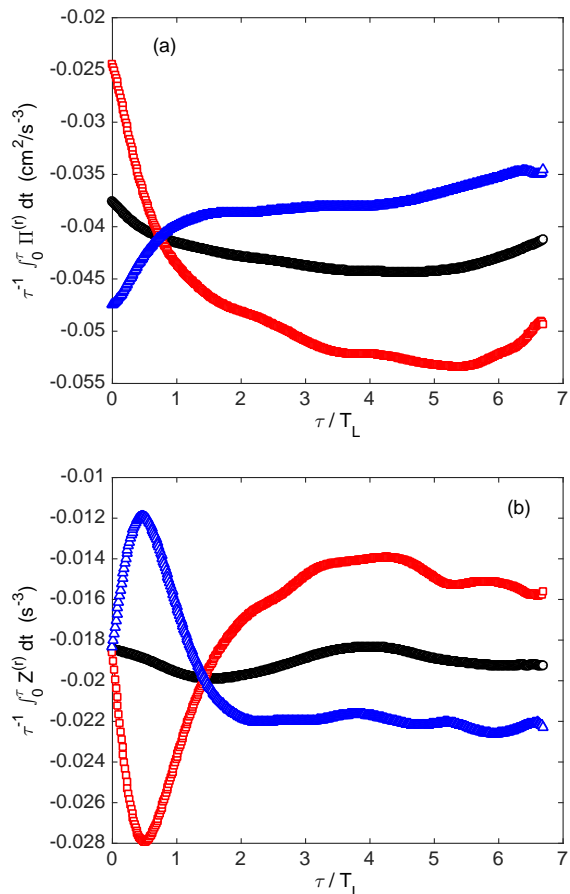


FIG. 4. (Color online) Time evolution of the Lagrangian averages of the (a) energy and (b) enstrophy fluxes at a fixed filter scale of  $r = 2L_m$ . Black circles denote unconditional averages; red squares are averages taken over particles that were initially in rotational regions, while blue triangles are for those that were initially in straining regions.

age of the total energy and enstrophy fluxes are nearly stationary in time, confirming our previous findings [14]. However, the Lagrangian averages of  $\Pi^{(r)}$  and  $Z^{(r)}$  conditioned on the *initial* value of  $\Lambda^{(r)}$  show very different behavior. Rather than being nearly stationary, the evolution of the Lagrangian averages is highly dependent on the initial character of the local flow field. At  $r = 1.5L_m$  (Figure 3), the Lagrangian average of both  $\Pi^{(r)}$  and  $Z^{(r)}$  increases markedly in initially straining regions, while decreasing sharply for initially rotational regions. The trend changes, however, as the averaging time increases. For  $\Pi^{(r)}$  the instantaneous enhancement seen for straining regions (see Figure 1) re-emerges after about one velocity integral time scale  $T_L$  (equal to 2.4 s in this data set). For  $Z^{(r)}$ , the distinction between initially straining and initially rotational regions begins to disappear for  $\tau \gg T_L$ , and eventually the conditional averages approach the unconditional average, although the enhancement due to strain persists for long times.

The situation is somewhat different for the larger filter

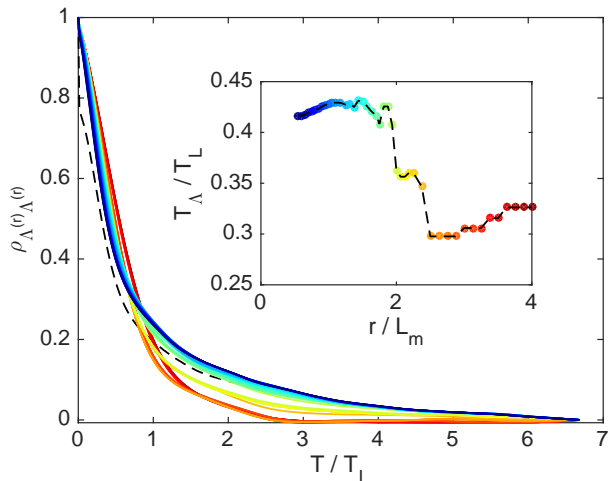


FIG. 5. (Color online) Lagrangian autocorrelation coefficient for the Okubo-Weiss parameter, filtered at different filter scales. The dashed black line shows the autocorrelation coefficient for the full (unfiltered) Okubo-Weiss parameter. The horizontal axis is normalized by  $T_L$ , the integral time scale for the velocity field. The inset shows the integral time scales for the different filter lengths. The colors of the symbols in the inset correspond to the filter scales used for the curves in the main panel.

scale,  $r = 2L_m$  (Figure 4). For  $\Pi^{(r)}$ , the initial enhancement in straining regions quickly gives way to stronger inverse fluxes in *rotational* regions. For  $Z^{(r)}$ , the trend is different. The initial enhancement of the weak inverse enstrophy flux in rotational regions grows for short times, but is eventually overtaken by an enhancement due to strain. This distinction persists for long times, even though the instantaneous conditional means for the enstrophy flux in this regime are the same as the unconditional mean (Figure 1).

### C. Lagrangian Correlations

To make sense of these results, we turn to the Lagrangian correlation functions. In Figure 5, we plot the Lagrangian autocorrelation coefficient  $\rho_{\Lambda^{(r)}\Lambda^{(r)}}(T)$  for the Okubo-Weiss parameter, defined as

$$\rho_{\Lambda^{(r)}\Lambda^{(r)}}(T) = \frac{\langle \Lambda^{(r)}(t)\Lambda^{(r)}(t+T) \rangle}{\langle \Lambda^{(r)}(t)^2 \rangle}, \quad (9)$$

where the averages are taken along Lagrangian trajectories, for a range of filter scales. As is typical with Lagrangian correlations, these curves fall off relatively rapidly; however, the rate at which they do depends on the filter scale. To measure the decay rate, we calculate the integral time scales  $T_\Lambda$ , defined as

$$T_\Lambda = \int_0^\infty \rho_{\Lambda^{(r)}\Lambda^{(r)}}(T) dT. \quad (10)$$

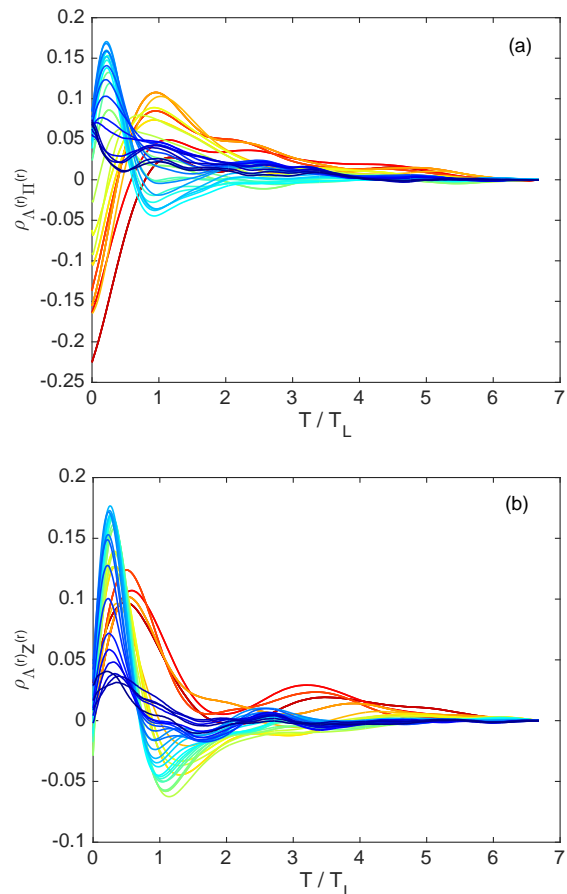


FIG. 6. (Color online) Lagrangian cross-correlations between the filtered Okubo-Weiss parameter and the (a) energy and (b) enstrophy fluxes. The colors are the same as in Figure 5.

We plot  $T_\Lambda$  as a function of  $r$  in the inset to Figure 5, scaled by the integral time scale  $T_L$  of the velocity field.  $T_\Lambda$  is smaller than  $T_L$  for all  $r$ ; however, it drops significantly for filter scales in the range where we observe net inverse energy flux. More importantly, however, the values of  $T_\Lambda$  we measure are similar to the times at which the Lagrangian averages of the energy and enstrophy fluxes peak in Figures 3 and 4. Thus, these data imply that the enhancement to the energy and enstrophy fluxes we see when averaging them along trajectories is a result of the finite correlation time of both the fluxes [12, 14] and the Okubo-Weiss parameter, and that the Lagrangian averages function as a “coherence filter” that reveal the net effects of this finite correlation.

We can also use Lagrangian correlation functions—in this case, cross correlations—to provide more information on how the Okubo-Weiss parameter is linked with the energy and enstrophy fluxes. We show in Figure 6 the Lagrangian cross correlations between the Okubo-Weiss parameter and  $\Pi^{(r)}$  and  $Z^{(r)}$  for different filter scales. For the energy flux (Figure 6(a)), we observe positive correlation at small filter scales. In this range, the mean

energy flux tends to be positive, again implying a net correlation between strain ( $\Lambda^{(r)} > 0$ ) and energy flux. At larger filter lengths, we observe instead anti-correlation at short times. In this range, however,  $\Pi^{(r)}$  is on the average negative, so this anti-correlation again implies that the energy flux is net correlated to strain. For the enstrophy, the picture is slightly different, as we do not observe anti-correlation at short times for large filter scales. This suggests that the small inverse transfer of enstrophy at large filter scales is correlated with rotation rather than strain. At first glance, this result may seem counter to previous work that showed a strong relationship between enstrophy flux and strain [8]; in that work, however, the authors fixed the filter scale to lie in the *forward* enstrophy cascade range, whereas here we find correlation with rotation only in the weak inverse enstrophy flux range.

#### IV. DISCUSSION AND CONCLUSIONS

Taken together, our results suggest that the sign of the instantaneous Okubo–Weiss parameter can be used both to determine (statistically) the character of the local spectral energy and enstrophy fluxes and their evolution in time. Consistent with earlier observations, we find that both types of fluxes are enhanced in regions that are predominantly straining, although the weak inverse enstrophy flux we observe eventually becomes stronger in rotational regions.

This result connecting the Okubo–Weiss parameter to the spectral dynamics of the flow may seem somewhat surprising, given that the Okubo–Weiss parameter has many known shortcomings. But our correlation analysis reveals why our results occur, particularly when combined with our earlier results on the Lagrangian correlations of the spectral fluxes themselves [12]. The correlation we see between  $\Lambda^{(r)}$ ,  $\Pi^{(r)}$ , and  $Z^{(r)}$  is not indicative of any deep relationship between the three; in particular, let us be clear that we are not arguing for a *causal* relationship between the instantaneous Okubo–Weiss parameter and the spectral properties of the flow. Rather, our results indicate that  $\Lambda^{(r)}$ ,  $\Pi^{(r)}$ , and  $Z^{(r)}$  are *independently* correlated with another quantity—the fluid advection itself [20]. Since all three persist along trajectories, instantaneous knowledge of one and of the correlations between them may provide information about the other two. This observation is likely linked to mesochronic analysis [32] and ergodic partitioning [33], and may be part of the reason why many different metrics for locating Lagrangian Coherent Structures (such as finite-time Lyapunov exponents or geodesic methods [13]) produce very similar results. Our results therefore suggest that, with appropriate Lagrangian averaging, quantities that have finite correlations along trajectories, frame-invariant or not, may find use in forecasting applications.

#### ACKNOWLEDGMENTS

This work was supported by the U.S. National Science Foundation under Grant No. DMR-1206399.

- 
- [1] A. K. M. F. Hussain, “Coherent structures and turbulence,” *J. Fluid Mech.* **173**, 303–356 (1986).
  - [2] G. L. Brown and A. Roshko, “On density effects and large structure in turbulent mixing layers,” *J. Fluid Mech.* **64**, 775–816 (1974).
  - [3] N. T. Ouellette, “On the dynamical role of coherent structures in turbulence,” *C. R. Physique* **13**, 866–877 (2012).
  - [4] M. Germano, “Turbulence: the filtering approach,” *J. Fluid Mech.* **238**, 325–336 (1992).
  - [5] S. Liu, C. Meneveau, and J. Katz, “On the properties of similarity subgrid-scale models as deduced from measurements in a turbulent jet,” *J. Fluid Mech.* **275**, 83–119 (1994).
  - [6] G. L. Eyink, “Local energy flux and the refined similarity hypothesis,” *J. Stat. Phys.* **78**, 335–351 (1995).
  - [7] M. K. Rivera, W. B. Daniel, S. Y. Chen, and R. E. Ecke, “Energy and enstrophy transfer in decaying two-dimensional turbulence,” *Phys. Rev. Lett.* **90**, 104502 (2003).
  - [8] S. Chen, R. E. Ecke, G. L. Eyink, X. Wang, and Z. Xiao, “Physical mechanism of the two-dimensional enstrophy cascade,” *Phys. Rev. Lett.* **91**, 214501 (2003).
  - [9] S. Chen, R. E. Ecke, G. L. Eyink, M. Rivera, M. Wan, and Z. Xiao, “Physical mechanism of the two-dimensional inverse energy cascade,” *Phys. Rev. Lett.* **96**, 084502 (2006).
  - [10] Z. Xiao, M. Wan, S. Chen, and G. L. Eyink, “Physical mechanism of the inverse energy cascade of two-dimensional turbulence: a numerical investigation,” *J. Fluid Mech.* **619**, 1–44 (2009).
  - [11] Y. Liao and N. T. Ouellette, “Spatial structure of spectral transport in two-dimensional flow,” *J. Fluid Mech.* **725**, 281–298 (2013).
  - [12] D. H. Kelley and N. T. Ouellette, “Spatiotemporal persistence of spectral fluxes in two-dimensional weak turbulence,” *Phys. Fluids* **23**, 115101 (2011).
  - [13] G. Haller, “Lagrangian coherent structures,” *Annu. Rev. Fluid Mech.* **47**, 137–161 (2015).
  - [14] D. H. Kelley, M. R. Allshouse, and N. T. Ouellette, “Lagrangian coherent structures separate dynamically distinct regions in fluid flows,” *Phys. Rev. E* **88**, 013017 (2013).
  - [15] A. Okubo, “Horizontal dispersion of floatable particles in the vicinity of velocity singularities such as convergences,” *Deep-Sea Res.* **17**, 445–454 (1970).
  - [16] J. Weiss, “The dynamics of enstrophy transfer in two-dimensional hydrodynamics,” *Physica D* **48**, 273–294 (1991).
  - [17] G. Haller, “An objective definition of a vortex,” *J. Fluid Mech.* **525**, 1–26 (2005).
  - [18] M. K. Rivera, H. Aluie, and R. E. Ecke, “The direct

- enstrophy cascade of two-dimensional soap film flows,” *Phys. Fluids* **26**, 055105 (2014).
- [19] M. R. Allshouse and J.-L. Thiffeault, “Detecting coherent structures using braids,” *Physica D* **241**, 95–105 (2012).
- [20] M. Farazmand, “Hyperbolic Lagrangian coherent structures align with contours of path-averaged scalars,” arXiv:1501.05036 (2015).
- [21] D. H. Kelley and N. T. Ouellette, “Onset of three-dimensionality in electromagnetically forced thin-layer flows,” *Phys. Fluids* **23**, 045103 (2011).
- [22] Y. Liao, D. H. Kelley, and N. T. Ouellette, “Effects of forcing geometry on two-dimensional weak turbulence,” *Phys. Rev. E* **86**, 036306 (2012).
- [23] Y. Liao and N. T. Ouellette, “Geometry of scale-to-scale energy and enstrophy transport in two-dimensional flow,” *Phys. Fluids* **26**, 045103 (2014).
- [24] N. T. Ouellette and J. P. Gollub, “Dynamic topology in spatiotemporal chaos,” *Phys. Fluids* **20**, 064104 (2008).
- [25] D. H. Kelley and N. T. Ouellette, “Using particle tracking to measure flow instabilities in an undergraduate laboratory experiment,” *Am. J. Phys.* **79**, 267–273 (2011).
- [26] N. T. Ouellette, H. Xu, and E. Bodenschatz, “A quantitative study of three-dimensional Lagrangian particle tracking algorithms,” *Exp. Fluids* **40**, 301–313 (2006).
- [27] N. Mordant, A. M. Crawford, and E. Bodenschatz, “Experimental Lagrangian probability density function measurement,” *Physica D* **193**, 245–251 (2004).
- [28] R. Ni, G. A. Voth, and N. T. Ouellette, “Extracting turbulent spectral transfer from under-resolved velocity fields,” *Phys. Fluids* **26**, 105017 (2014).
- [29] R. H. Kraichnan, “Inertial ranges in two-dimensional turbulence,” *Phys. Fluids* **10**, 1417–1423 (1967).
- [30] C. E. Leith, “Diffusion approximation for two-dimensional turbulence,” *Phys. Fluids* **11**, 671–673 (1968).
- [31] G. K. Batchelor, “Computation of the energy spectrum in homogeneous two-dimensional turbulence,” *Phys. Fluids* **12**, II233–II239 (1969).
- [32] I. Mezić, S. Loire, V. A. Fonoberov, and P. Hogan, “A new mixing diagnostic and Gulf oil spill movement,” *Science* **330**, 486–489 (2010).
- [33] M. Budišić and I. Mezić, “Geometry of the ergodic quotient reveals coherent structures in flows,” *Physica D* **241**, 1255–1269 (2012).